International Journal of Plasticity 171 (2023) 103800

Contents lists available at ScienceDirect

International Journal of Plasticity

journal homepage: www.elsevier.com/locate/ijplas

Microstructural insights into fatigue short crack propagation resistance and rate fluctuation in a Ni-based superalloy manufactured by laser powder bed fusion

Jianghua Li [a], Qinghui Huang [a], Zhiyang Wang [b,*], Ningyu Zhang [a], Gang Chen [c], Guian Qian [a,*]

[a] State Key Laboratory of Nonlinear Mechanics (LNM), Institute of Mechanics, Chinese Academy of Sciences, Beijing 100190, China
[b] Australian Nuclear Science and Technology Organisation (ANSTO), Sydney, NSW 2234, Australia
[c] School of Chemical Engineering and Technology, Tianjin University, Tianjin, China

ARTICLE INFO

Keywords:
Ni-based superalloy
Fatigue short cracks
Microstructure
Propagation model

ABSTRACT

The microstructural sensitivity of fatigue short crack path and its propagation rate in a Ni-based superalloy GH4169 manufactured by laser powder bed fusion (LPBF) was investigated at room temperature. In-situ digital image correlation (DIC) observation and post-mortem microstructural analysis around the crack path were performed. The results show that the intragranular cracks developed in the shear cracking mode are closely aligned along the activated slip bands in the γ-matrix grains with the crystallographic characteristics of parallel to the γ-{111} slip planes. Multiple slip was also activated, causing the crack retardation or deflection. Low-angle grain boundaries and subgrain boundaries were shown to cause deflections of intragranular cracking, while high-angle grain boundaries significantly arrested the short crack propagation. Moreover, the resistance of grain boundaries to short cracking was assessed using combined metrics including the crystallographic and microstructural parameters of twist angle, the Schmid factor and the geometrical compatibility factor. These site-specific microstructural analyses around the crack path provide insights into the microstructural origins of resistance to the short crack propagation as well as an interpretation of the observed significant fluctuations in the crack propagation rate.

1. Introduction

GH4169 alloy (equivalent to the American brand Inconel® 718) is a precipitation-hardened Ni-based superalloy, extensively used in the aerospace, chemical and nuclear industries due to its comprehensive properties including high tensile strength, fatigue and creep strength, outstanding corrosion resistance required for a range of severe conditions (Deng et al., 2021). The complexity of the structural components in these applications entails challenges and high costs associated with materials manufacturing. Effective manufacturing approaches beyond traditional processes are increasingly needed for materials and components production with time, cost and resources saving advantages. Additive manufacturing (AM, or 3D printing) has emerged as a promising technique to this end due to its inherent advantages of freeform manufacturing and assembly through consolidation of additive raw materials. Among

* Corresponding authors.
E-mail addresses: zhiyangw@ansto.gov.au (Z. Wang), qianguian@imech.ac.cn (G. Qian).

https://doi.org/10.1016/j.ijplas.2023.103800
Received 21 August 2023; Received in revised form 22 October 2023;
Available online 4 November 2023

various AM processes, laser powder bed fusion (LPBF) is a prevalent technique utilizing the laser beam for the consolidation of metallic powders in a layer-by-layer manner. Due to extremely high cooling rates, the LPBF-produced metallic materials often show interesting microstructure such as fine lamellar (Liu et al., 2023a,b) and cellular structures (Bean et al., 2022), as well as enhanced mechanical properties compared to counterparts by traditional manufacturing.

The fatigue performance is often linked to the microstructure of the AM material and needs to be investigated before the practical applications of AM components. Previous studies indicate that the fatigue endurance of AM Inconel 718 is inferior to its wrought counterpart, especially at high strain amplitudes (Gribbin et al., 2016; Johnson et al., 2016). This is primarily attributed to the presence of brittle precipitates or defects in the as-printed materials. Compared with the as-printed material, Inconel 718 alloy after solution annealing showed better fatigue endurance. This is interpreted as the sub-micron cell structures after solution annealing efficiently suppresses the dislocation movement imposed by the cyclic loading (Aydinöz et al., 2016). Of particular notice is that during high cycle or very high cycle fatigue a large fraction of the fatigue life is consumed in the initiation and propagation of microstructurally short cracks defined with a length scale up to approximately 1 mm (Taylor and Knott, 1981). The fatigue short crack propagation is a technically important process over the whole fatigue lifetime. The mechanistic understanding of this process remains challenging, due to its sensitivity to local microstructure.

The fatigue short crack propagation rate is generally affected by the occurrence of crack deflection and branching (Barat et al., 2022; Wang et al., 2023b; Zhang and Dunne, 2023). Consequently, short fatigue cracks grow at a fluctuating rate due to their interaction with the microstructural barriers. Unlike the long cracks, which generally grow at an increasing rate with increasing the stress intensity factor range, ΔK, the short fatigue cracks propagate in a non-linear manner (Davidson et al., 2003). Fatigue short cracks are shown to grow faster than large cracks at the same nominal ΔK. They may even propagate at the nominal applied ΔK below the threshold value, ΔK_{th}, a phenomenon known as the short crack effect (Taylor and Knott, 1981).

In the microstructural scale, the fatigue short cracking involves the processes of persistent slip band formation, crack-grain boundary interaction, precipitation and crack branching (Song et al., 2022; Texier et al., 2016, 2019). Fatigue studies in single-crystal Ni-base superalloys indicated that short cracks grow along the crystallographic planes (the so-called shear cracking mode) (Wang et al., 2023c). In polycrystalline alloys, crack paths are also influenced by grain boundary. Masakazu et al. (1990) found that cracks propagated along the crystallographic slip planes, and the propagation rate rapidly decreased as they approached grain boundaries. The resistance of grain boundaries to fatigue short cracking was observed to be stronger for those with large boundary misorientations (Schaef et al., 2011). In addition, the growth of short cracks is often retarded or even arrested by secondary phase particles in the microstructure (Mbuya et al., 2017).

An improved understanding of the relationship between the microstructure heterogeneity and the resulting fatigue performance needs to be established before the widespread application of AM structural materials and components. The knowledge is also vital for developing models for the prediction of fatigue short crack propagation rate and remaining lifetime. Therefore, this work investigated the propagation behavior of short fatigue cracks (less than 1 mm in length) in AM GH4169 alloy at room temperature. A detailed microstructure analysis was carried out to reveal the mechanisms of short fatigue crack propagation. Lastly, an improved short crack propagation model was proposed taking account of the microstructure heterogeneity.

2. Experimental procedures

2.1. Samples

The GH4169 Ni-based superalloy materials were manufactured using a commercial EP-M250 LPBF system. Round bars ($\Phi 15 \times 120$ mm) were manufactured with the bar length direction parallel to the build direction. The chemical composition of the GH4169 alloy powder used in LPBF is listed in Table 1. The following processing parameters were used for printing: laser power 240 W, scan speed 1000 mm/s, and layer thickness 40 μm. A bidirectional scanning strategy (Piglione et al., 2021) with 45° rotations between the successive layers was applied during LPBF.

It is known that the brittle Laves phase and δ phase may form during LPBF due to micro-segregation of Nb and Ti at a fast-cooling rate (Zhao et al., 2021), while the precipitation of fine γ'' and γ' secondary phases required for enhanced mechanical properties of this Ni-based alloy is often suppressed in the as-built condition. Therefore, we performed a proper post heat treatment following Ref. Huang et al. (2021) to dissolve the Laves and δ phases and introduce the favorable precipitates to enhance the mechanical properties of the LPBF Ni-based alloy. The as-built LPBF GH4169 round bars were solution annealed at 980 °C for 1 h to promote the dissolution of the Laves and δ phases, and subsequently double aged at 720 °C for 8 h and 620 °C for 8 h, respectively, to promote the precipitation of both γ'' and γ' phases. In this study, all the samples were investigated in this heat-treatment condition.

Table 1
Chemical composition of GH4169 alloy powders (wt.%) used in LPBF.

Ni	Cr	Nb	Mo	Ti	Al	Co	C	Si	Cu	Fe
52.08	20.12	5.33	3.24	0.99	0.54	0.056	0.036	0.038	0.013	Bal.

2.2. Tensile and fatigue tests

Quasi-static tensile tests were carried out at room temperature on the heat-treated LPBF GH4169 alloy specimens with the loading direction parallel to the build direction. Fig. 1(a) shows the geometry of the specimens for quasi-static tensile tests. In accordance with the ASTM E8/E8M-11 standard, the tensile tests were conducted at a nominal strain rate of $2.5 \times 10^{-4}\ s^{-1}$ using an MTS hydraulic testing machine with the load capacity up to 50 kN. The strain was measured by a uniaxial extensometer attached to the tensile specimens. Two repeated tensile tests were conducted to check the repeatability of the measurements.

Single-notched (R1) plate specimens for the fatigue tests, as schematically shown in Fig. 1(b), were machined out from the heat-treated round bar materials. Two sides of the fatigue specimens were polished before testing. The final thickness of the specimens is approximately 0.6 mm. Considering the thin specimen geometry, a plane stress condition can be assumed for the present high cycle fatigue tests. The stress concentration factor, K_t, is determined to be ~3 by the finite element (FE) method. The inset in Fig. 1(b) shows an enlarged contour plot of the FE-calculated normal axial stress distribution near the notch of the fatigue specimen. A significant tensile stress concentration at the center position of the notch is predicted from the FE calculation.

In-situ fatigue crack propagation measurements were conducted using a uniaxial testing system equipped with a 2D digital image correlation (DIC) facility, developed by the CARE Measurement & Control, Co. Ltd. A camera with the pixel size of 4.5 μm and a resolution of 110 lp/mm was used in the DIC imaging system. Fig. 2(a) shows the applied fatigue testing system. All the fatigue tests were carried out at room temperature, under the load control mode using a triangle wave with a frequency of 5 Hz and a stress ratio R ($\sigma_{min}/\sigma_{max}$) of 0.1. Two individual fatigue tests were carried out with stress amplitudes of 157.5 MPa and 135 MPa, respectively. During the fatigue testing, the evolutions of the crack length and the strain field around a crack tip were monitored by DIC. For this purpose, speckle patterns of random white dots on the black background are prepared on one side of the specimen, as shown in Fig. 2 (b). The speckle density was measured by the ImageJ software, showing an average distance between intense particles in the speckle patterns of approximately 57 μm. A spatial resolution of about 10 μm is achieved in the present DIC displacement measurement with the applied speckle pattern and DIC imaging system, which is sufficient for the observation of fatigue short crack propagation. To capture the evolution of fatigue short cracks (defined with the length less than 1 mm), digital images were taken continuously at a rate of one image per 50 cycles under the corresponding maximum stress until the crack length reaches about 1 mm.

The short fatigue crack propagation rate can be calculated from the slope (da/dN) of the crack length (a) vs. fatigue cycle (N) plot, i.e. the length increment per fatigue cycle, given by:

$$(da/dN)_i = \frac{a_{i+1} - a_i}{N_{i+1} - N_i} \tag{1}$$

The stress intensity factor range (ΔK) for a single-notched plate of finite width is given by:

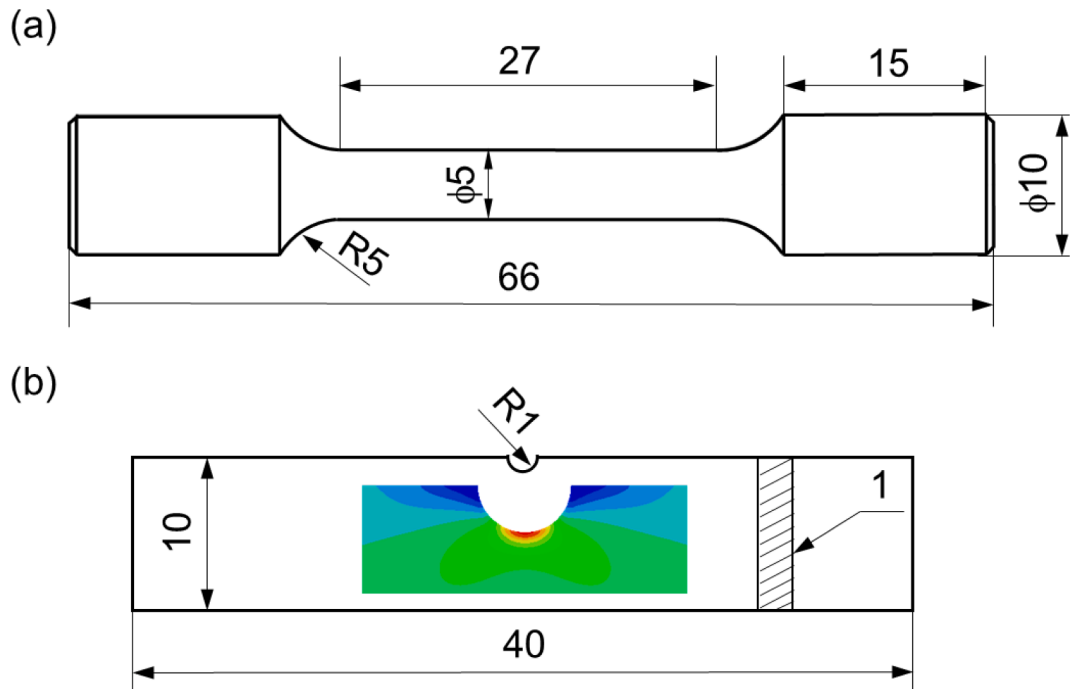

Fig. 1. The geometries of specimens for the (a) quasi-static tensile tests and (b) fatigue tests. The length direction of the specimens is parallel to the build direction. The inset in (b) is an enlarged contour plot showing the axial stress distribution near the notch of tensile deforming specimen, obtained from the FE simulation.

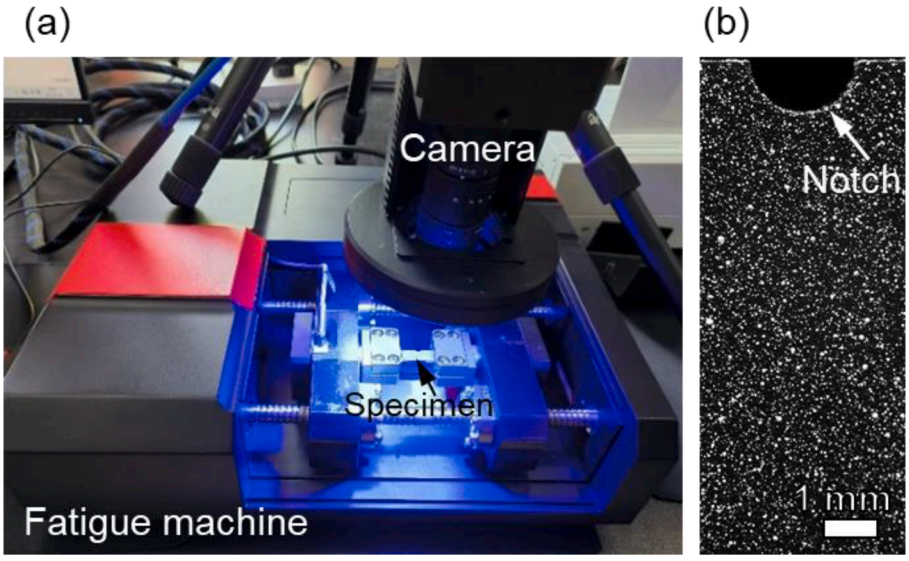

Fig. 2. (a) Experimental setup for in-situ fatigue testing with a 2D DIC measurement system, (b) typical speckle patterns prepared on the surface of the fatigue specimen.

$$\Delta K = \Delta\sigma\sqrt{\pi(a+b)}F(\xi) \tag{2}$$

where $\Delta\sigma$ is the stress range, the crack length a is defined as the projected length vertical to the loading axis, b is the depth of notch, and $\xi = a/W$ (W is the width of specimen). $F(\xi)$ is a coefficient defined as Wang and Fan (2006):

$$F(\xi) = 0.265(1-\xi)^4 + (0.857 + 0.265\xi)(1-\xi)^{-3/2} \tag{3}$$

2.3. Microstructure characterization

The microstructures of the heat treated LPBF GH4169 alloy specimens before and after fatigue tests were characterized by Electron Backscatter Diffraction (EBSD) using a Zeiss Gemini 300 Scanning Electron Microscope (SEM) operated at 20 kV. The specimens for EBSD observations were mechanically polished to 1 μm SiC sandpaper, followed by fine polishing using a 0.05 μm colloidal suspension solution for 30 min. Detailed characterization of the fatigue crack propagation paths of the specimens after fatigue tests was performed by SEM and EBSD. The obtained EBSD data were analyzed using the HKL Channel 5 software. Additionally, X-ray diffraction (XRD) analysis was conducted to identify the strengthening precipitation phases in the specimens before fatigue. The XRD data were collected using a PANalytical X'Pert Pro X-ray diffractometer with Cu Kα radiation source and analyzed by Pawley refinement to confirm the precipitates using the TOPAS v4.2 program (Coelho, 2018).

3. Results and discussion

3.1. Initial microstructure

Before fatigue testing, the initial microstructure of the heat-treated LPBF GH4169 alloy was characterized, and the results are shown in Fig. 3. As presented in Fig. 3(a), the EBSD orientation map shows a gradual color variation within the grains, indicating the existence of local misorientation in the initial microstructure. Fig. 3(b) shows the EBSD-measured histogram of the boundary misorientation distribution. It is observed from Fig. 3(b) that a significant amount of low-angle grain boundaries (LAGBs) with the dominant misorientation of ~5° developed in the initial microstructure, while the high-angle grain boundaries (HAGBs) show a range of misorientation spreading from 15° to ~63°. A large amount of LAGBs existed in the microstructure of GH4169 is consistent with previous observations of significant local misorientation typically developed in the microstructure of AM materials due to the thermal cycling of extremely fast heating and cooling experienced during manufacturing (Wang et al., 2023a). In addition, the EBSD result reveals the heterogeneous microstructure of the samples with the grain sizes distributed in a range of ~20 to ~50 μm.

Fig. 3(c) further shows the measured XRD pattern and the Pawley refinement of initial sample. In addition to the γ-matrix phase (space group $Fm\bar{3}m$), the γ′ ($Pm\bar{3}m$), and γ″ ($I4/mmm$) precipitates were identified. As shown in the inset in Fig. 3(c), the overlapped peaks of these phases, such as γ (111), γ′ (111) and γ″ (112) in the Bragg angle range of approximately 43° to 45°, were deconvoluted by the Pawley refinement analysis. Further evidence of these precipitates is presented in the backscattered electron images in Fig. 3(d), demonstrating the relatively homogeneous distribution of strengthening phases of spherical γ′ and disc-shaped γ″ precipitates. Moreover, the γ matrix grains show the fine lamellar subgrain structure, the microstructural characteristics as observed in many other

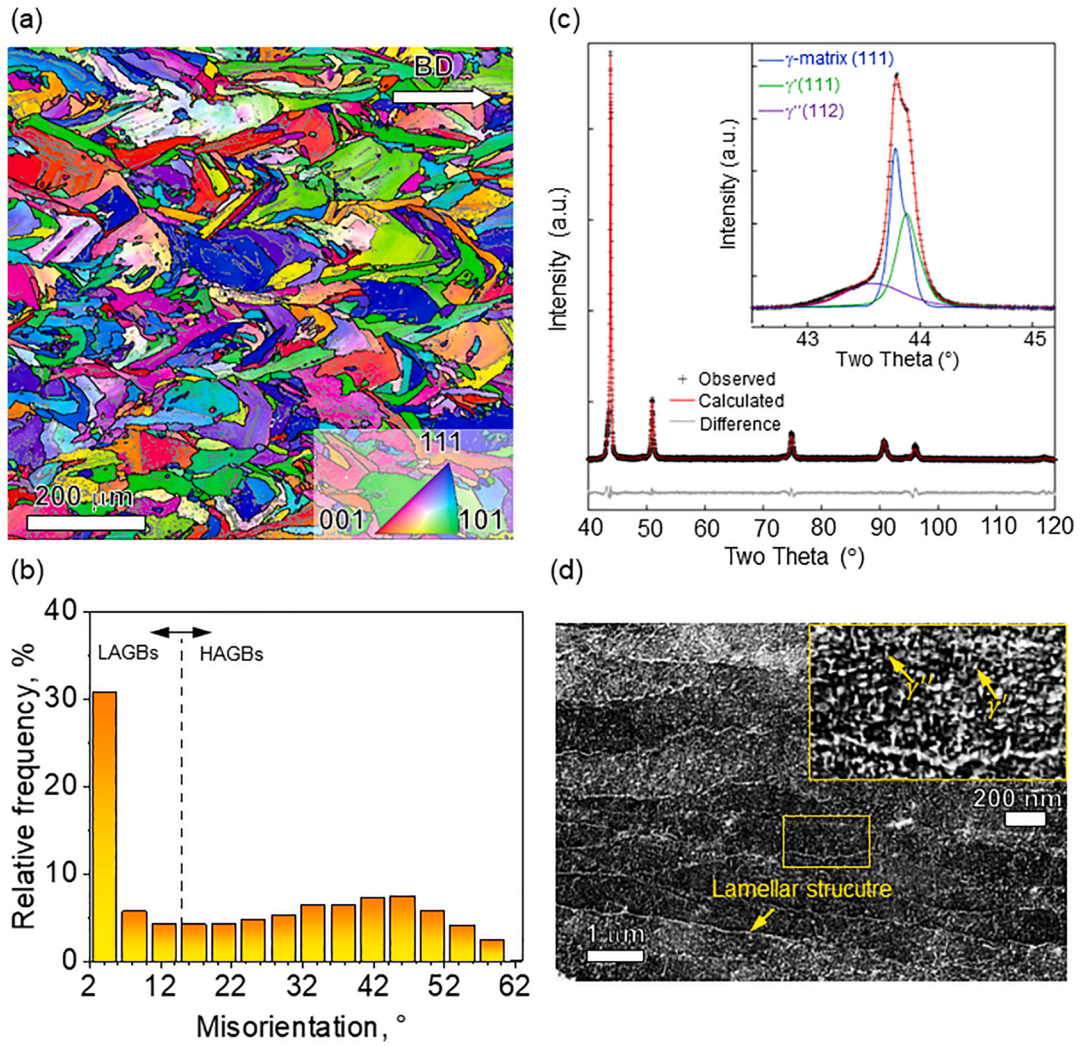

Fig. 3. Initial microstructure of the heat-treated LPBF GH4169 alloy: (a) EBSD-based IPF orientation map measured along the build direction. The LAGBs with the misorientation (θ) in a range of 2° to 15° and the HAGBs ($15° \leq \theta \leq 62.8°$) are highlighted in gray and black, respectively. (b) Grain boundary misorientation distribution. (c) Pawley refinement of the XRD data confirming the presence of γ' and γ'' precipitates. (d) Backscattered electron images showing the fine subgrain structure of γ matrix and the precipitates.

LPBF alloys such as Inconel 718, 316L steel and Al-Si alloy (Cui et al., 2021; Li et al., 2020; Zhao et al., 2021).

3.2. *Quasi-static tensile properties*

The fatigue performance of metallic alloys is highly correlated with their tensile properties. Hence, we first measured the tensile properties of the heat-treated GH4169 alloy at room temperature before the fatigue testing. The resultant typical tensile engineering stress-strain curve is shown in Fig. 4(a). The measurements show the yield strength (YS) of 1265 MPa, the ultimate tensile strength (UTS) of 1415 MPa, and the elongation at the fracture of 16.4%. We further compared the tensile properties of the LPBF GH4169 alloy in this study with those of LPBF Inconel 718 alloy reported previously (Huang et al., 2021, 2019; Wang et al., 2012). These data are shown in Fig. 4(b). The comparison suggests that the investigated LPBF GH4169 alloy in this study shows a combination of high strength and ductility at room temperature, which are comparable to those of LPBF Inconel 718 alloy in previous reports (Huang et al., 2021, 2019; Wang et al., 2012).

3.3. *Fatigue short crack propagation observation*

The fatigue tests were subsequently performed with a focus on the observation of short crack propagation behavior. Fig. 5(a)–(c) show the DIC-measured crack length evolution and longitudinal strain (ε_{xx}) distribution near the developed dominant crack at three fatigue stages under a stress amplitude of 135 MPa. The magnitude of tensile strain is shown to increase with increasing fatigue cycles

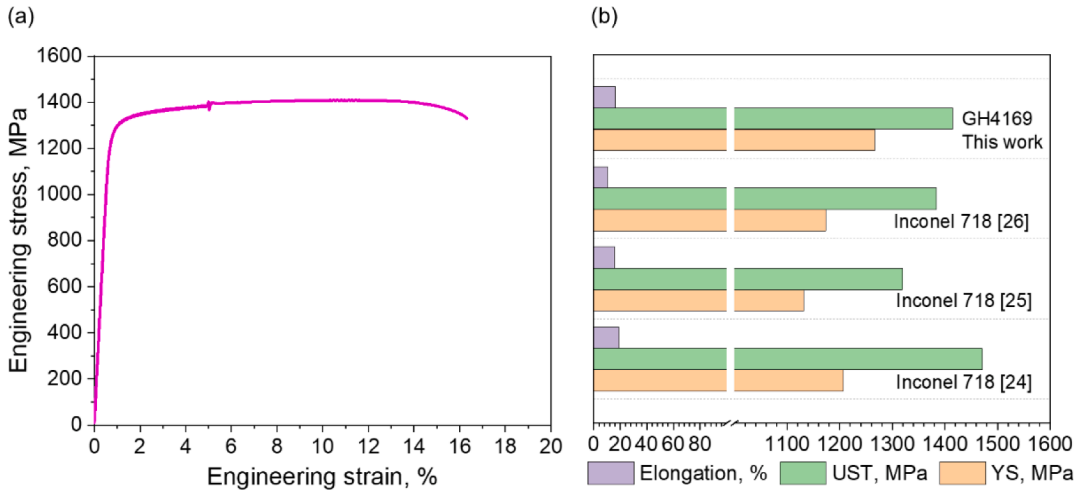

Fig. 4. (a) Typical engineering stress-strain curve of LPBF GH4169 alloy from the tensile tests at room temperature, (b) tensile properties including the elongation, the ultimate tensile strength (UTS) and the yield strength (YS) of the LPBF GH4169 from this work, together with those of LPBF Inconel 718 alloy reported in the literature (Huang et al., 2021, 2019; Wang et al., 2012).

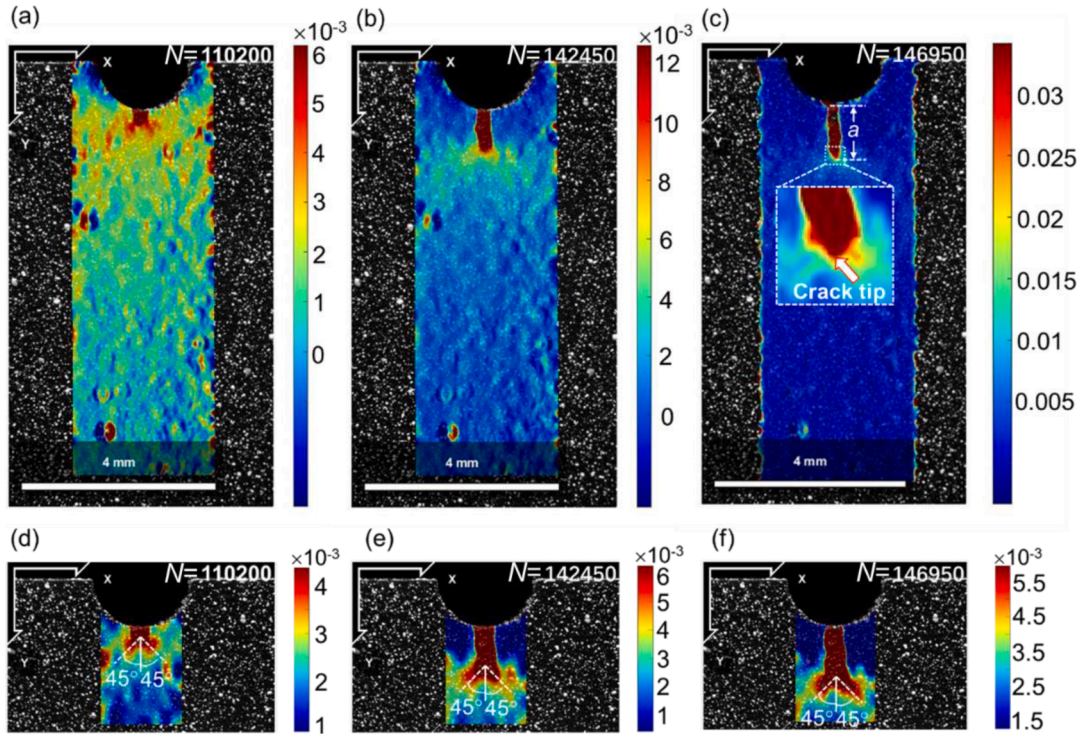

Fig. 5. DIC-measured longitudinal strain ε_{xx} distribution under the stress amplitude of 135 MPa showing the crack length at various fatigue cycles (N) of (a) 110,200, (b) 142,450, and (c) 146,950. (d, e) show the corresponding localized contour plots for (a–c) respectively, highlighting the local strain accumulation and distribution around the notch.

(N). The maximum strain intensity criterion (Mahmoudi et al., 2023; Liu et al., 2023a,b; Hannes et al., 2022) was used to define the evolving crack length from a plastic activity during the fatigue process, and the crack tip is identified as the location where local strain showed significant drops, as indicated in the inset in Fig. 5(c). Moreover, with the progression of fatigue cycling a tensile strain concentration develops in a small region near the crack tip and shows a distribution along two directions of about ±45° away from the fatigue crack propagation path (Fig. 5(d)–(f)). Such strain concentration at the crack tip is further aggravated with the increase of fatigue cycles. At $N = 146{,}950$ cycles, the longitudinal strain ε_{xx} at the crack tip reaches about 0.6%, which is above the proof yield strain of 0.2% and indicative of the plastic deformation occurred locally at this location. At the microstructural scale, the development

of micro-cracks with fatigue cycling is likely associated with significant stress concentration, resulting in the plastic deformation near the cracks.

In-situ DIC observations during the fatigue testing allow the quantitative measurements of the crack propagation and the results are shown in Fig. 6. In the case of crack branching occurred during the fatigue testing, the crack length is measured as the length of main crack. Fig. 6(a) presents the evolutions of crack length (a) as a function of fatigue cycles (N) under the stress amplitudes of 157.5 and 135 MPa. Longer fatigue life at higher stress amplitude (157.5 MPa) is found compared to the case of low stress amplitude (135 MPa). Such counterintuitive behavior is likely due to the large scatter of the stress magnitude and fatigue cycle data often seen in AM materials Murakami et al., 2021). The presence of defects in AM materials may cause the localization of plasticity during fatigue loading, promoting the initiation of fatigue cracks. Additionally, the actual notch geometry and machining accuracy of the investigated fatigue samples may lead to sample-to-sample variations in the level of stress concentration during fatigue loading. Both factors may contribute to the scatter in the stress magnitude and fatigue cycle data and the present observation of shorter fatigue lifetime at lower stress magnitude (Fig. 6(a)), as supported by previous work (Solber et al., 2019). Moreover, it appears that there is an overall trend of accelerated crack growth at the increased crack length, however, the crack propagation rate does not increase linearly with increasing the crack length at both stress amplitudes. The local variation of the fatigue crack propagation rate (da/dN) is determined from the a-N data in Fig. 6(a). The stress intensity factor range ΔK is then calculated according to Eqs. (1)–((3). Fig. 6(b) plots the obtained fatigue short crack propagation rates da/dN as a function of ΔK under the stress amplitude of 135 MPa and 157.5 MPa. It shows that both the short crack propagation rates under two stress magnitudes show significant fluctuation in a range of $\sim 2 \times 10^{-9}$ m/cycle to $\sim 1 \times 10^{-7}$ m/cycle (Fig. 6(b)). Such behavior of irregular short crack growth rates is distinctive from the scenario of fatigue long cracking where the corresponding propagation rate normally increases linearly with increasing ΔK (Gruber et al., 2023; Kim et al., 2020; Ostergaard et al., 2022). The resistance of the crack retardation is measured by $\Delta da/dN$, as shown in Fig. 6(b). Here, $\Delta(da/dN)$ is the difference in da/dN between the onset of fatigue crack deceleration and the local minimum point. $\Delta da/dN$ acts as a measure of the crack growth resistance, and the larger the $\Delta da/dN$, the larger the crack growth resistance. The $da/dN - \Delta K$ data in Fig. 6(b) suggests that the crack growth resistance changes in the crack propagation process as shown by the variation of $\Delta da/dN$.

In addition, the fatigue short crack rate curves (Fig. 6(b)) under the different stress amplitudes exhibit a similar profile. This is because the fatigue crack propagation rate is predominantly dependent on the applied stress ratio (R) at the test temperature (Suzuki et al., 2022), which is the same ($R = 0.1$) for two stress amplitudes applied in this work.

3.4. *Multiple slip associated with the fatigue crack branching*

Fig. 7 presents the SEM micrographs around the crack propagation path under the stress amplitude of 157.5 MPa. An overview of the cracking path together with the corresponding plot of the crack growth rate evolution with the stress intensity factor range are presented in Fig. 7(a). Note that macroscopically the fatigue crack tends to propagate perpendicularly to the load direction, while microscopically crack deflection and branching consistently occur which indicate the blocking of main crack propagation. It is known that fatigue short cracking is more sensitive to local microstructure than the long crack propagation, and consequently a correlation between the microstructure features and the variation of fatigue short cracking rate is often observed in various alloy systems (Kim et al., 2020; Lu et al., 2023). To clarify the microstructural origin of the variation in the fatigue short crack propagation rate during cycling, we performed detailed inspections of the corresponding crack sites (indicated by the letters A-F in the inset of Fig. 7(a)) along the crack propagation path with local minima of the propagation rate. The high-magnification backscattered electron images around three sections of the crack propagation path are shown in Fig. 7(b)–(e) and described in detail below.

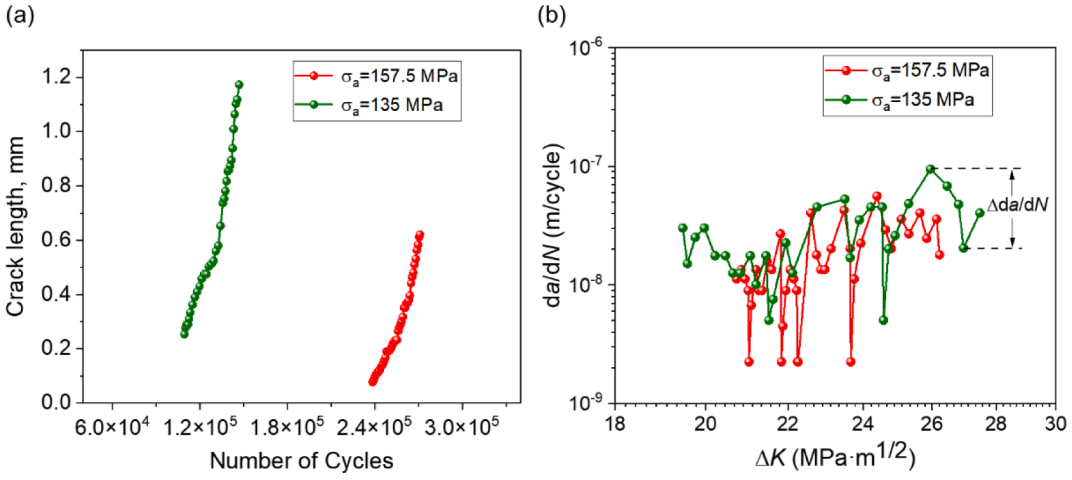

Fig. 6. Fatigue short crack propagation observations in LPBF GH4169 alloy under the stress amplitudes of 157.5 and 135 MPa: (a) Crack length evolutions as a function of the number of cycles, and (b) fatigue short crack propagation rate da/dN versus the stress intensity range ΔK.

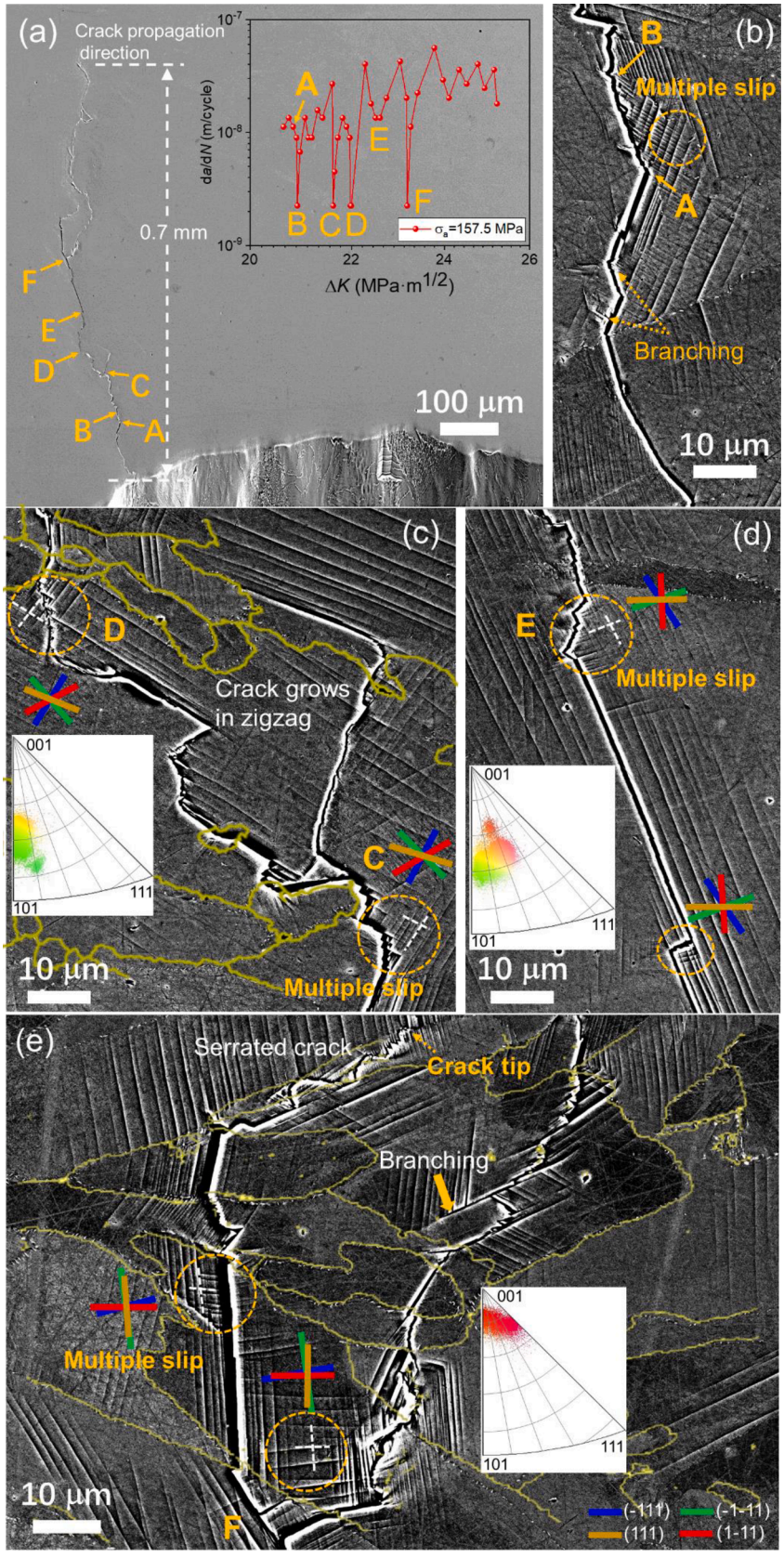

(caption on next page)

Fig. 7. (a) An overview of fatigue short cracks up to a length of 0.75 mm at a stress amplitude of 157.5 MPa. The inset in (a) is a plot of the fatigue short crack propagation rate da/dN versus the stress intensity range ΔK curve at 157.5 MPa. Data points with significant decrease in the crack propagation rate are marked by letters (A-F) in the inset in (a), and the corresponding marked letters are indicated in the crack propagation path in (a). Backscattered electron images in (b–e) show a sequence of enlarged views of cracks along the propagation direction developed at different stages of fatigue.

(i) Fig. 7(b) presents the microstructure near the A-B section along the cracking path. It reveals that the local fatigue crack propagates along the slip bands, showing the straight cracking path. However, the crack propagation is substantially impeded along the A-B section (Fig. 7(b)), and the serrated crack surfaces are observed. This cracking path consumes about 1600 fatigue cycles. In addition, significant multiple slip is observed around the A-B crack section. In this circumstance, some small crack branches develop along with the main crack as it propagates, exhibiting hierarchical characteristics, as shown by the dotted circle in Fig. 7(b). Note that such multiple slip frequently occurs around the entire crack propagation path (Fig. 7(b)–(e)), which is found to be accompanied with the resultant arrest or deflection of the main crack.

(ii) Fig. 7(c) shows the microstructure near the section C-D of the fatigue short crack growth path. The zigzag cracking path extended along the main crack propagation direction is observed in this section. The HAGBs are highlighted by the yellow curves in Fig. 7(c). The observation shows that near the region C the main crack first propagates around a grain boundary, followed by a brief horizontal intergranular propagation accompanied by two crack branches extended approximately vertical to the applied loading direction. The main crack further propagates along the activated slip bands in the grain. It has been suggested that the three-dimensional geometries of the cracks and the grain boundaries in the microstructure may affect the surface crack propagation behavior (Liu et al., 2022), resulting in multiple deflections of the crack, and hence the zigzag propagation path as shown in Fig. 7(c). When the moving crack encounters the adjacent grain boundary, the crack propagation is arrested due to the blocking effect induced by the grain boundary misorientation, resulting in the activation of local multiple slip, same as the observation in region C (Fig. 7(c)). To understand the crystallographic features of the activated multiple slip, the orientations of relevant grains around the crack are illustrated in the inverse pole figure in Fig. 7(c). The {111} plane traces on the sample surface are determined, as shown by the white lines in Fig. 7(c), and these slip traces are found closely parallel to the (−1–11) and (−111) planes of the γ-matrix crystals.

(iii) Fig. 7(d) shows the intragranular crack propagation along the slip bands, observed in the main crack section near the location E. Two crack deflections are observed in this section, both of which are accompanied by multiple slips, as highlighted by dotted circles. In addition, as shown in Fig. 7(e), near the region marked by letter F, the crack branches also develop along the bands of

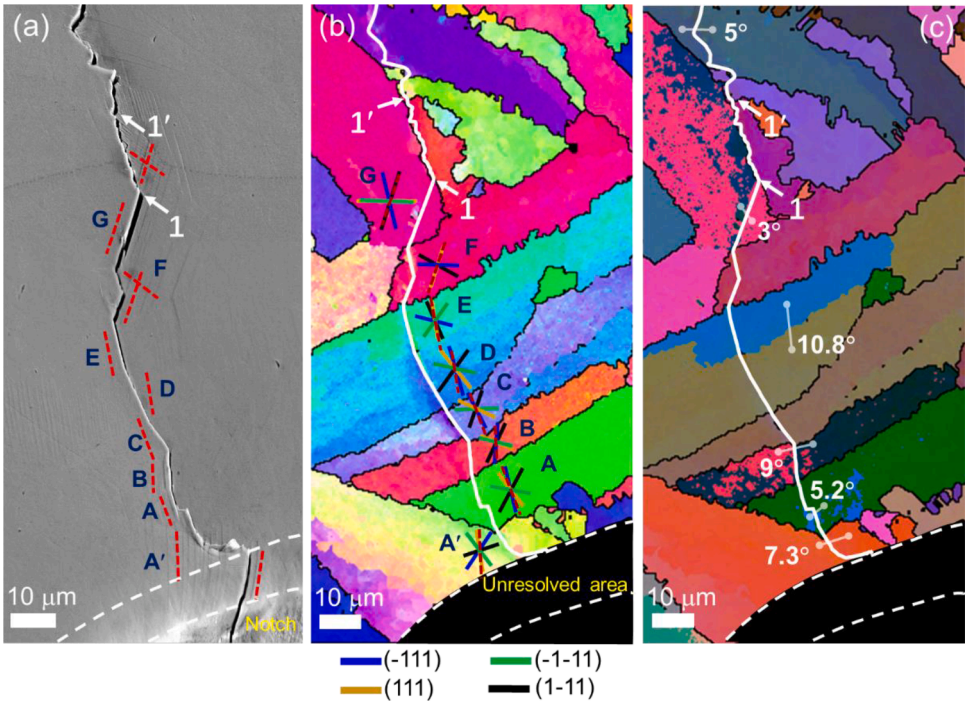

Fig. 8. (a) SEM and (b, c) EBSD observations of the cracks near the notch. The EBSD-based orientation maps in (b) and (c) are presented using the IPF and all Euler angle coloring schemes, respectively. The persistent slip bands are marked by red lines in a and b. The deviation angle between the activated slip plane in the grain and the corresponding intragranular crack path is within 3°, except for grains A, C and D, where deviation angles are about 12°, 8° and 13°, respectively.(For interpretation of the references to color in this figure legend, the reader is referred to the web version of this article.)

the multiple slip. The left branch of the crack readily propagates, while the right branch of the crack is blocked within the grain. The left branch first grows along the produced slip bands. When the crack propagation encounters the grain boundary, as indicated by the dotted circles, multiple slip occurs. The crack path in the adjacent grain shows certain deflection and does not follow the activated slip bands. Finally, the crack growth is retarded, showing a serrated crack surface, and the crack tip is indicated by the dash arrow in Fig. 7(e) (see the detailed analysis in Section 2 of the Supplementary Material). Therefore, after 1200 loading cycles, the right crack branch began to grow, and gradually merged with the main crack after about 4000 cycles (see the detailed analysis in Section 1 of the Supplementary Material). Obvious plastic deformation around the right branch of the crack and multiple slip is observed, as indicated by the dotted circles in Fig. 7(e). The orientations of the involved grains are shown in the inverse polar figure and found to be close to γ-[001] crystallographic direction, so the angle between the multiple slip traces is approximately 90°.

It is considered that in addition to the grain boundaries, the abundant fine γ' and γ'' precipitates existed in the microstructure may also affect the fatigue short crack development in the investigated alloy. Especially, when the γ''/γ' precipitates are arranged as the blocks in a fine regular morphology, the generated γ''/γ interface may further exacerbate the dislocation pileup (Yu et al., 2021b; Zhao et al., 2021). In addition, the γ'' precipitation is well recognized as the principal strengthening phase partially due to its large coherency strain (~3%) with the γ matrix (Campbell, 2008). Particularly the large-sized γ'' particles can act as strong barriers to dislocation motion, making it difficult for them to be sheared or bowed by dislocations during the plastic deformation (Zhao et al., 2020). Hence, we performed additional observations of secondary-phase particles in the vicinity of the crack paths, and the collected typical BSE images are shown in Fig. S3 of the Supplementary. We had close inspections of these precipitates near the crack paths in Fig. S3(a) to understand their interaction with the cracks. These fine precipitates are observable at relatively high magnification of SEM observation. As representatively shown in Fig. S3(b), the secondary cracks do not seem to initiate or develop at the sites of these small precipitates. Instead, it is observed in Fig. S3(b) that the secondary crack tends to propagate along the slip band. That is, the present observations do not show appreciable effect of these secondary-phase particles on the crack development. Limited by the present experimental resolution, the exact role of these fine precipitates on the fine-scale crack formation cannot be unambiguously determined in this study. Consequently, we believe that local inhomogeneous slip deformation is the dominant factor influencing the stress concentration and associated crack development. The resultant local dislocation pileup or stress concentration due to the precipitates may promote local crack deflection, as shown in Fig. 7(d).

3.5. *Microstructure sensitivity of fatigue short crack propagation*

To reveal the correlation between the fatigue short crack propagation path and grain orientations, SEM-EBSD mapping was performed over the cracking region near the notch and the results are shown in Fig. 8. The SEM observation in Fig. 8(a) indicates that the main crack initiates from the notch root of the fatigue specimen due to local stress concentration as shown in Fig. 2(b). Consistent with previous observations in Fig. 7, the crack path is closely aligned along the persistent slip traces marked by red lines in Fig. 8(a), (b). This is because the emerging slip bands on the specimen surface during fatigue loading provide initial sites of stress concentration and cause the localized strain with ongoing fatigue cycling, as observed by SEM-based DIC measurements in previous work (Jiang et al., 2017). Therefore, these slip bands facilitate the crack initiation and propagation (Polák et al., 2017). Additionally, straight cracks are often observed (Fig. 8(a)) which are rationalized as the crack propagation along the crystallographic slip planes near the specimen surface (known as the “shearing mode” (Suzuki et al., 2022)). In the face-centered-cubic (FCC) crystals like GH4169 alloy, dislocation glide often occurs with the most common {111}⟨110⟩ slip system. After fatigue cycling many persistent slip bands appeared near the cracks due to significant extrusions of the crack flanks (Fig. 7(b)–(e)). Fig. 8(b) and (c) further show the corresponding EBSD

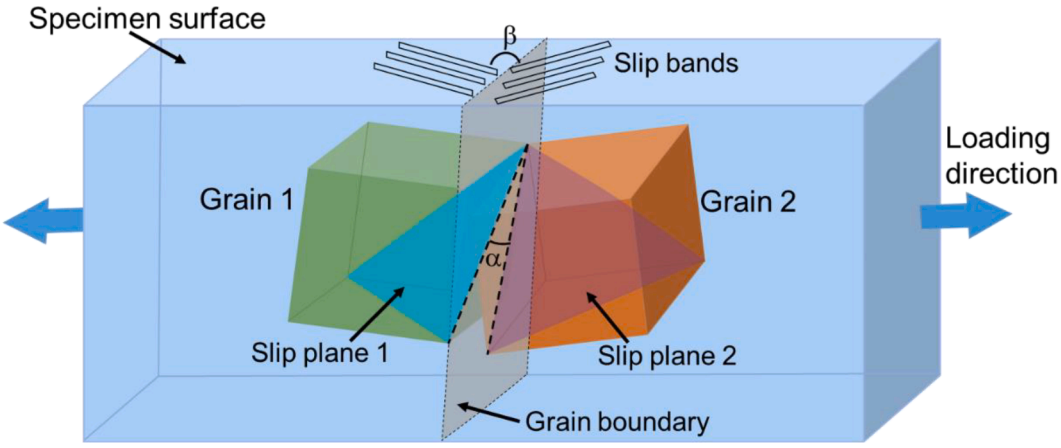

Fig. 9. Schematic illustration showing the definition of crystallographic parameters of twist angle α and tilt angle β proposed by Zhai et al. (2000). α is the angle between the slip traces on the grain boundary, and β is the angle between the two slip traces at the observation surface.

orientation maps for Fig. 8(a). The slip trace analysis based on these EBSD observations confirms that these fatigue short cracks tend to propagate along the γ-{111} crystallographic planes and deflections of crack paths occur due to multiple slip (see Fig. 7(d), (e)). Notice that the LAGBs with local misorientations below 15° (Fig. 8(c)) appears to have an appreciable effect on the shearing crack propagation, showing a slight deflection of the intragranular cracks, such as in grain A′, A and D-E.

Moreover, it is found that when the shearing crack on the specimen surface encountered a grain boundary as marked by the arrow 1 in Fig. 8, it transitioned to the intergranular mode. This transition in the cracking mode is believed to be associated with the low obstruction resistance to cracking of this grain boundary. The grain boundaries from 1 to 1′ are approximately perpendicular to the loading direction, which provide favorable paths for the cracks. However, it should be noted that the interaction between zigzag grain boundaries and multiple activated slip planes in adjacent grains leads to wavy crack paths and crack growth retardation (as shown in Fig. 8(a)). The transition from shearing mode crack to opening crack mode around the grain boundary accompanied by the crack retardation has also been reported in previous in-situ observations (Suzuki et al., 2022).

The propagation of microstructurally short cracks was found to be governed by the easy slip transfer paths across the grain boundaries (Larrouy et al., 2015; Zhai et al., 2000). A crystallographic model has been developed to interpretate the crack-plane twist and tilt effects on the fatigue crack resistance at the grain boundaries (Zhai et al., 2000). As schematically illustrated in Fig. 9 the tilt angle (β) is defined as the angle between the traces of the slip planes on the surface and twist angle (α) is the angle between traces of the slip planes and the grain boundary plane that is assumed to be perpendicular to the surface plane. This model analysis revealed that twist and tilt angles of the crack-plane is the key factor controlling the short crack growth. The slip planes oriented with small tilt angle β and twist angle α are favorable paths for the short crack propagation due to their low resistance to the crack growth under this orientation configuration (Zhai et al., 2000). When the advancing crack propagates into the slip planes with smaller tilt and twist angles than previous ones (i.e. the crack-plane configuration with reduced resistance), the crack deflection would take place, as seen in Fig. 7. Otherwise, the crack propagation will be arrested or slowed down at the crack-planes with high resistance to crack growth characterized by high tilt and twist angles. We believe that the significant fluctuation of the short crack propagation rate observed in Fig. 6(b) is highly correlated with the wide spread of the grain boundary misorientations in initial microstructure (Fig. 3(b)) which show varying resistance to the crack propagation.

The twist angle α of the slip planes along the cracks is further calculated following the crystallographic model (Zhai et al., 2000), and the result is listed in Table 2. It is found that most intragranular cracks (Fig. 7) tend to grow along the slip planes with small twist angles, i.e., generally following the minimum twist angle criterion for the fatigue crack propagation. The fatigue short cracks are prone to propagate when the twist angle α and tilt angle β are less than 40° and 60°, respectively. Conversely, the slip planes characterized by large α over 40° are more resistant to intergranular propagation. This finding is consistent with previous reports on various structural

Table 2
The grain orientation (represented by three Euler angles), Schmid factor, twist (α) and tilt (β) angles of the slip planes in grains A′-G marked in Fig. 8.

Euler angles (°)	Slip planes	α (°)	β (°)	Schmid factor	m'
A′	(111)			0.4400	
333.1, 30.4, 12.8	(−111)			0.4659	
	(11–1)			0.4317	
	(1–11)			0.2632	
A	(111)	2.18	30	0.4039	
24.3, 36.4, 1.8	(− 111)	68.18	6.06	0.4748	0.13
	(11–1)	88.74	12.06	0.1526	
	(1–11)	49.49	36.18	0.4031	
B	(111)	53.89	53	0.2332	
4.5, 16.5, 24.3	(− 111)	14.09	17.98	0.4901	0.49
	(11–1)	3.53	62.57	0.2085	
	(1–11)	84.27	39.56	0.4814	
C	(111)	41.85	69.29	0.1404	
194.7, 38, 29.6	(− 111)	79	31.8	0.4540	0.38
	(11–1)	77.61	83.93	0.0373	
	(1–11)	19.77	15.17	0.3709	
D	(111)	63.78	10.95	0.2165	
179.9, 42.9, 29	(− 111)	3.2	11.79	0.4853	0.96
	(11–1)	65.62	48.91	0.2178	
	(1–11)	58.46	63.4	0.4858	
E	(111)	73.82	37.01	0.3328	
5.4, 42.5, 68.6	(−111)	52.91	29.44	0.2256	
	(11–1)	47.18	81.57	0.4676	
	(1–11)	4.16	21.98	0.4996	0.97
F	(111)	16.48	11.03	0.4453	0.69
256, 20.5, 43	(−111)	46.75	85.99	0.0244	
	(11–1)	55.75	9.82	0.3224	
	(1–11)	87.89	66.2	0.3774	
G	(111)	33.13	73.04	0.0005	
355.6, 22.7, 47.9	(−111)	88.72	30.24	0.4072	
	(11–1)	41.86	75.07	0.0336	
	(1–11)	22.43	0.26	0.4240	0.80

materials of hexagonal close packed (HCP) (Zeng et al., 2022) and FCC structures (Jiménez et al., 2019; Park et al., 2023; Wen et al., 2016), suggesting that this crystallographic parameter of twist angle is an intrinsic and general metric for the fatigue short cracking resistance.

Furthermore, based on the EBSD-measured grain orientation data, the Schmid factors of the grains in Fig. 8(b) are calculated and listed in Table 2. Herein, the Schmid factor of a slip plane is defined as the largest one of all the three slip systems on the crystallographic planes, and the corresponding slip traces of {111} planes are indicated by different color lines, as shown in Fig. 8(b). Interesting, the results show that in addition to the crystallographic characteristics of small twist angles, the slip planes favorable for the short crack propagation are often associated with higher Schmid factor.

Another consideration is that the fatigue crack generally propagates along directions of easy slip transfer in the microstructure, irrespective of its orientation with respect to the applied load. Hence, we evaluate the other microstructural parameter, the geometrical compatibility factor (m'), on its applicability for the characterization of fatigue short crack propagation. This m' factor characterizes the ease of slip transfer across adjacent grains and quantifies the accommodation of plastic deformation. It is defined as $m' = cos\varphi \cdot cos\psi$ (Luster and Morris, 1995), where φ is the angle between the normal directions of slip planes in adjacent grains, and ψ is the corresponding angle between slip directions.

The higher m', the easier for the dislocation slip to pass through the grain boundary and hence favoring the crack propagation. In other words, the lower m' indicates a higher resistance of grain boundary against slip transfer which leads to local stress concentration due to the strain incompatibility. The m' values of adjacent grains showing intergranular fatigue crack in Fig. 8 are calculated and the results are listed in Table 2. Similar to the Schmid factor result, the intergranular fatigue short cracking tends to occur at the grain boundaries of higher m' value larger than 0.3 (Table 2). Overall, our detailed site-specific microstructural analysis around fatigue short cracks reveals that the fatigue crack propagation is governed by complex interplay between the fatigue deformation and grain-scale characteristics, and the microscopic resistance to the fatigue short cracking in the studied alloy can be measured by a few synergistic crystallographic and microstructural parameters including the twist angle, Schmid factor and geometrical compatibility factor.

3.6. Fatigue short crack propagation modeling

It is known that a linear relationship between the fatigue short crack propagation rate and the stress intensity factor range has been described in a few models such as Shyam model (Shyam et al., 2005) and modified Paris law (Santus and Taylor, 2009). However, most of the existing models are derived assuming elastic perfectly plastic materials, and the influence of microstructure inhomogeneity and local yield strength on the fatigue crack propagation was not considered. Therefore, to account for the variation of local yield strength of grains in the plastic zone created near the cracks during the fatigue process, local yield strength (σ_{ym}) has been proposed as a microscopic parameter governing the local yielding behavior (Chan and Lankford, 1988). Ye et al. (2017) developed the calculation formulation of σ_{ym}, assuming that σ_{ym} in the plastic zone around the cracks obeys the Hall–Petch type relationship:

$$\sigma_{ym} = \sigma_0 + (\sigma_y - \sigma_0)\sqrt{1 - \left(1 + \frac{\delta}{\delta D}\right)\exp\left(-\frac{a}{\delta D}\right)} \tag{4}$$

where σ_0 is the fatigue strength of the material, σ_y is the macroscopic yield strength, D is the average grain size, a is the crack length and δ is a coefficient (taken as 1.5 Ye et al. (2017) in this study) which reflects the rate of transition from microstructurally short crack to long crack.

Combined with the modified stress intensity factor range ΔK^* proposed by Chan and Lankford (1988), a crack growth model taking

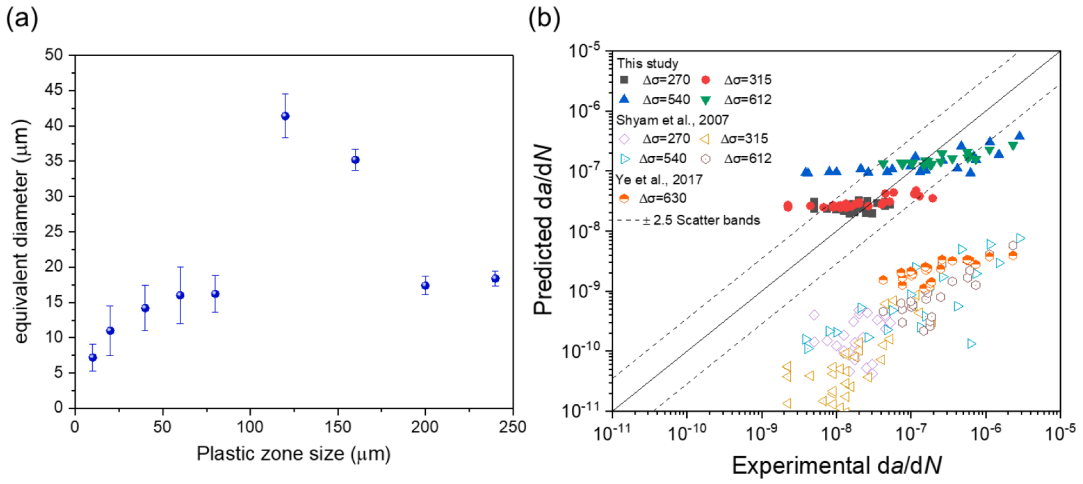

Fig. 10. (a) Equivalent grain diameter under instant crack-tip plastic zone, and (b) Predictions of the crack growth rate based on the present model, Shyam model (Shyam et al., 2007) and Ye model (Ye et al., 2017), plotted together with the corresponding experimental data.

account of local yield strength has been developed to describe the short crack growth behavior (Ye et al., 2017). The formulation is as follow:

$$\frac{da}{dN} = C(\Delta K^* - \Delta K_{ths})^m \tag{5}$$

$$\Delta K^* = \Delta K \cdot q \tag{6}$$

$$q = 1 + \frac{4\sqrt{2}}{\pi}\frac{\sigma_y}{\Delta\sigma}\sqrt{\frac{r_{pc}}{a}}\left(1 - \frac{\sigma_{ym}}{\sigma_y}\right) \tag{7}$$

where C and m are empirical constants, r_{pc} is the cyclic plastic zone size expressed as $r_{\mathrm{pc}} = a\left(\sec\left(\frac{\pi\sigma_{\max}(1-R)}{4\sigma_{ys}}\right) - 1\right)$ (Shyam et al., 2005), $\sigma_{\max}$ is the maximum stress. ΔK_{ths} is the short crack intensity factor range expressed as $\Delta K_{ths} = \Delta K_{th}\sqrt{\frac{a}{a+d}}$, where ΔK_{th} is the threshold of long crack intensity factor range, and d is a constant (El Haddad et al., 1979), which is given as $d = \frac{1}{\pi}\left(\frac{\Delta K_{th}}{\sigma_0}\right)^2$, herein $\sigma_0 = 306$ MPa is taken in this study following Ref. Yu et al. (2021a).

Note that the average grain size D in the crack-tip plastic zone is usually assumed to be equal to the average grain size of the materials with homogeneous microstructure in the short crack growth rate models Wang et al., 2021; Ye et al., 2017). The traditional assumption method is not appropriate for the presently studied AM alloy with inhomogeneous microstructure (Fig. 3(a)). Hence, a proper analysis of the average grain size D in the plastic zone is needed in this modeling. As shown in Fig. 10(a), the evolution of equivalent grain diameter D as a function of crack-tip plastic zone size under different fatigue stages is evaluated and considered in the present analytical modeling of short crack propagation rate (see Eqs. (4)–((7)).

The present modeling takes account of the local yield strength and inhomogeneous grains in the crack-tip plastic zone and the prediction results of crack growth rate are shown in Fig. 10(b). To better validate of the proposed model, additional fatigue tests at the stress magnitudes of 540 and 612 MPa were included in Fig. 10(b). It shows that our prediction results are in reasonable agreement with the experimental data. In addition, the present model is compared with previous ones (Fig. 10(b)), including a linear crack propagation model proposed by Shyam et al. (2007) to calculate the accumulated crack-tip opening displacement and the microscopic model proposed by Ye et al. (2017) that only considers the correlation of crack length. The comparison results show that the prediction results using previous models (Shyam et al., 2007; Ye et al., 2017) which did not consider local microstructure are conservative.

Short surface cracks are more susceptible to microstructural effects than long cracks because of the different numbers of grains encountered at their crack tips (Davidson et al., 2003). The number of grains encountered by a small crack of initial length, embedded within a single grain is unity. As the short crack length increases, the number of grains along the crack front increases proportionally, and ultimately reaching the length scale of a long crack. Because of the sampling effect, the mechanical properties (e.g., yield stress, etc.) of the crack-tip plastic zone ahead of a short crack vary with crack length and get closer to those of a long crack (average properties) as the crack length increases. Therefore, the present modeling considering the inhomogeneous microstructure improves the prediction of fatigue short crack growth rate.

In addition, it should be mentioned that only the surface characterization of the short crack progression was allowed in this work from the present DIC measurements. Due to this technical limitation, the sub-surface crack observations were not available from this study. However, based on previous work (e.g., Miao et al., 2009), the internal fatigue crack in the early stage of fatigue was also initiated and propagated along {111} slip planes of a Ni-based superalloy. Therefore, crystallographic {111} facets are usually observed in fatigue fractographic studies (Zhang and Takahashi, 2023; Suzuki et al., 2022). It is speculated that the propagation paths of the sub-surface cracks are like those of surface cracks for Ni-based alloys, i.e., tend to follow the activated slip planes. Despite this, without the solid experimental evidence of sub-surface cracking, we are not able to validate if the cracking model we proposed for surface crack progression is applicable in the bulk volume of the fatigue samples.

4. Conclusions

The fatigue short crack propagation behavior in a Ni-based superalloy GH4169 manufactured by LPBF was investigated in this work. Single-notched samples were used in the fatigue testing at room temperature. In-situ digital image correlation (DIC) measurements during the fatigue process were performed to quantify the short crack development. Post-mortem microstructural analysis around the crack path was conducted to correlate the microstructural characteristics and evolutions during fatigue with the observed significant fluctuations in the crack propagation rate. In addition, improved microstructure-sensitive fatigue short crack propagation modeling was presented. The main conclusions are summarized below:

(1) The intragranular short cracks developed in the shearing crack mode tend to propagate closely along the slip bands generated in the vicinity of the crack path. These activated slip bands show the crystallographic characteristics of aligned parallel to the γ-matrix {111} slip planes, resulting in many straight crack sections. The retardation or deflection of intragranular cracks also occurs which is induced by multiple slip. Moreover, the LAGBs and subgrain boundaries also have an appreciable effect on the intragranular shearing crack propagation.
(2) Grain boundaries show significant blocking effect on the crack propagation which are dependent on their orientations. The resistance of grain boundaries to the propagation of microstructurally short cracks was evaluated by a few crystallographic and

microstructural parameters including the twist angle, the Schmid factor, and the geometrical compatibility factor. The fatigue short cracks are shown to favorably propagated through the grain boundaries oriented with the twist angle less than 40°.

(3) The short crack propagation rate exhibits remarkable fluctuations. The deceleration of crack propagation rate is mainly related to the blocking effects of grain boundaries as well as the plasticity event of multiple slip around the crack path leading to the retardation or deflection of cracks path.

(4) An improved analytical modeling of crack propagation taking account of the local yield strength and evolving crack-tip plastic zone size is presented. The modeling allows reasonable prediction of fatigue lifetime in the studied condition. However, limitations do exist for this modeling, and comprehensive microstructural parameters need to be considered in future efforts to interpretate the crack rate fluctuation in the short cracking stage.

Declaration of Competing Interest

The authors declare that they have no known competing financial interests or personal relationships that could have appeared to influence the work reported in this paper.

Data availability

Data will be made available on request.

Acknowledgements

This work was supported by the National Natural Science Foundation of China (Fund nos. 12072345, 11932020, 12202444), National Science and Technology Major Project (J2019-VI-0012-0126) and Science Center for Gas Turbine Project (P2022-B-III-008-001), and China Postdoctoral Science Foundation (no. 2021M693240). Special thanks are due to Prof. Youshi Hong for his insightful discussion and instruction.

Supplementary materials

Supplementary material associated with this article can be found, in the online version, at doi:10.1016/j.ijplas.2023.103800.

References

Aydinöz, M.E., Brenne, F., Schaper, M., Schaak, C., Tillmann, W., Nellesen, J., Niendorf, T., 2016. On the microstructural and mechanical properties of post-treated additively manufactured Inconel 718 superalloy under quasi-static and cyclic loading. Mater. Sci. Eng. 669, 246–258.

Barat, K., Ghosh, A., Doharey, A., Mukherjee, S., Karmakar, A., 2022. Crystallographic evaluation of low cycle fatigue crack growth in a polycrystalline Ni based superalloy. Int. J. Plast. 149, 103174.

Bean, C., Wang, F., Charpagne, M.A., Villechaise, P., Valle, V., Agnew, S.R., Gianola, D.S., Pollock, T.M., Stinville, J.C., 2022. Hetergeneous slip localization in an additively manufactured 316L stainless steel. Int. J. Plast. 159, 1034436.

Campbell, F., 2008. Elements of Metallurgy and Engineering Alloys. ASM International-Technology & Engineering. Chapter 14.

Chan, K.S., Lankford, J., 1988. The role of microstructural dissimilitude in fatigue and fracture of small cracks. Acta Metall. 36, 193–206.

Coelho, A.A., 2018. TOPAS and TOPAS-academic: an optimization program integrating computer algebra and crystallographic objects written in C++. J. Appl. Crystallogr. 51, 210–218.

Cui, L.Q., Jiang, S., Xu, J.H., Peng, R.L., Mousavian, R.T., Moverare, J., 2021. Revealing relationships between microstructure and hardening nature of additively manufactured 316L stainless steel. Mater. Des. 198, 109385.

Davidson, D., Chan, K., McClung, R., Hudak, S., 2003. 4.05—Small fatigue cracks. In: Milne, I., Ritchie, R.O., Karihaloo, B. (Eds.), 4.05—Small fatigue cracks. Comprehensive Structural Integrity 129–164.

Deng, D.Y., Peng, R.L., Moverare, J., 2021. High temperature mechanical integrity of selective laser melted alloy 718 evaluated by slow strain rate tests. Int. J. Plast. 140, 102974.

El Haddad, M.H., Topper, T.H., Smith, K.N., 1979. Prediction of non-propagation cracks. Eng. Fract. Mech. 11, 573–584.

Gribbin, S., Bicknell, J., Jorgensen, L., Tsukrov, I., Knezevic, M., 2016. Low cycle fatigue behavior of direct metal laser sintered Inconel alloy 718. Int. J. Fatigue 93, 156–167.

Gruber, K., Szymczyk-Ziółkowska, P., Dziuba, S., Duda, S., Zielonka, P., Seitl, S., Lesiuk, G., 2023. Fatigue crack growth characterization of Inconel 718 after additive manufacturing by laser powder bed fusion and heat treatment. Int. J. Fatigue 166, 107287.

Hannes, P., Paul, K., Manuela, S., 2022. Fatigue crack growth determination under in-phase and out-of-phase mixed-mode loading conditions using an automated DIC evaluation tool. Int. Fatigue 164, 107122.

Huang, W., Yang, J., Yang, H., Jing, G., Wang, Z., Zeng, X., 2019. Heat treatment of Inconel 718 produced by selective laser melting: microstructure and mechanical properties. Mater. Sci. Eng. 750, 98–107.

Huang, L., Cao, Y., Zhang, J., Gao, X., Li, G., Wang, Y., 2021. Effect of heat treatment on the microstructure evolution and mechanical behaviour of a selective laser melted Inconel 718 alloy. J. Alloys Compd. 865, 158613.

Jiang, R., Pierron, F., Octaviani, S., Reed, P.A.S., 2017. Characterisation of strain localisation processes during fatigue crack initiation and early crack propagation by SEM-DIC in an advanced disc alloy. Mater. Sci. Eng. 699, 128–144.

Jiménez, M., Ludwig, W., Gonzalez, D., Molina-Aldareguia, J.M., 2019. The role of slip transfer at grain boundaries in the propagation of microstructurally short fatigue cracks in Ni-based superalloys. Scr. Mater. 162, 261–265.

Johnson, A.S., Shao, S., Shamsaei, N., Thompson, S.M., Bian, L., 2016. Microstructure, fatigue behavior, and failure mechanisms of direct laser-deposited Inconel 718. JOM 69, 597–603.

Kim, S., Choi, H., Lee, J., Kim, S., 2020. Room and elevated temperature fatigue crack propagation behavior of Inconel 718 alloy fabricated by laser powder bed fusion. Int. J. Fatigue 140, 105802.
Larrouy, B., Villechaise, P., Cormier, J., Berteaux, O., 2015. Grain boundary-slip bands interactions: impact on the fatigue crack initiation in a polycrystalline forged Ni-based superalloy. Acta Mater. 99, 325–336.
Li, Z., Li, Z., Tan, Z., Xiong, D.B., Guo, Q., 2020. Stress relaxation and the cellular structure-dependence of plastic deformation in additively manufactured AlSi10Mg alloys. Int. J. Plast. 127, 102640.
Liu, C., Thomas, R., Sun, T., Donoghue, J., Zhang, X., Burnett, T.L., da Fonseca, J.Q., Preuss, M., 2022. Multi-dimensional study of the effect of early slip activity on fatigue crack initiation in a near-α titanium alloy. Acta Mater. 233, 117967.
Liu, D.K., Chen, H.N., Su, R.K.L., Chen, L.J., Liang, K., 2023a. Influence of initial crack length on fracture properties of limestone using DIC technique. Constr. Build. Mater. 403, 133020.
Liu, K., Yan, Z., Wang, F., Li, K., Lin, S., Chen, S., 2023b. Microstructure, texture and mechanical properties of Inconel GH4169 superalloy fabricated by wire arc additive manufacturing with arc oscillation. J. Alloys Compd. 952, 170070.
Lu, D.D., Lin, B., Liu, T.L., Deng, S.X., Guo, Y.J., Li, J.F., Liu, D.Y., 2023. Effect of grain structure on fatigue crack propagation behavior of Al-Cu-Li alloys. J. Mater. Sci. Technol. 148, 75–89.
Luster, J., Morris, M.A., 1995. Compatibility of deformation in two-phase Ti-Al alloys dependence on microstructure and orientation relationships. Metall. Mater. Trans. A 26, 1745–1756.
Mahmoudi, A., Khosravani, M.R., Khonsari, M.M., Reinicke, T., 2023. On the evaluation of entropy threshold for debonding during crack propagation using DIC technique. Eng. Fract. Mech. 288, 109361.
Masakazu, O., Tetsuo, T., Shinichiroh, N., 1990. Intrinsic stage I crack growth of directionally solidified Ni-Base superalloys during low-cycle fatigue at elevated temperature. Metall. Trans. A 21, 2201–2208.
Mbuya, T.O., Gu, Y., Thomson, R.C., Reed, P.A.S., 2017. Effect of intermetallic particles and grain boundaries on short fatigue crack growth behaviour in a cast Al-4Cu-3Ni-0.7Si piston alloy. Fatigue Fract. Eng. Mater. Struct. 40, 1428–1442.
Miao, J.S., Pollock, T.M., Jones, J.W., 2009. Crystallographic fatigue crack initiation in nickel-based superalloy René 88DT at elevated temperature. Acta Mater 57, 5964–5974.
Murakami, Y., Takagi, T., Wada, K., Matsunaga, H., 2021. Essential structure of S-N curve: prediction of fatigue life and fatigue limit of defective materials and nature of scatter. Int. J. Fatigue 146, 106138.
Ostergaard, H.E., Pribe, J.D., Tarik Hasib, M., Paradowska, A.M., Siegmund, T., Kruzic, J.J., 2022. Near-threshold fatigue crack growth in laser powder bed fusion produced alloy 718. Int. J. Fatigue 163, 107041.
Park, S., Tanaka, Y., Okazaki, S., Funakoshi, Y., Kawashima, H., Matsunaga, H., 2023. Inferior fatigue resistance of additively-manufactured Ni-based superalloy 718 and its dominating factor. Int. J. Fatigue 176, 107801.
Piglione, A., Attard, B., Vieira Rielli, V., Santos Maldonado, C.-T., Attallah, M.M., Primig, S., Pham, M.-S., 2021. On the constitutive relationship between solidification cells and the fatigue behaviour of IN718 fabricated by laser powder bed fusion. Addit. Manuf. 47, 102347.
Polák, J., Mazánová, V., Heczko, M., Petráš, R., Kuběna, I., Casalena, L., Man, J., 2017. The role of extrusions and intrusions in fatigue crack initiation. Eng. Fract. Mech. 185, 46–60.
Santus, C., Taylor, D., 2009. Physically short crack propagation in metals during high cycle fatigue. Int. J. Fatigue 31, 1356–1365.
Schaef, W., Marx, M., Vehoff, H., Heckl, A., Randelzhofer, P., 2011. A 3-D view on the mechanisms of short fatigue cracks interacting with grain boundaries. Acta Mater. 59, 1849–1861.
Shyam, A., Allison, J., Jones, J., 2005. A small fatigue crack growth relationship and its application to cast aluminum. Acta Mater. 53, 1499–1509.
Shyam, A., Allison, J.E., Szczepanski, C.J., Pollock, T.M., Jones, J.M., 2007. Small fatigue crack growth in metallic materials: a model and its application to engineering alloys. Acta Mater. 55, 6606–6616.
Solberg, K., Berto, F., 2019. Notch-defect interaction in additively manufactured Inconel 718. Int. J. Fatigue 122, 35–45.
Song, K., Wang, K., Zhang, L., Zhao, L., Xu, L., Han, Y., Hao, K., 2022. Insights on low cycle fatigue crack formation and propagation mechanism: a microstructurally-sensitive modeling. Int. J. Plast. 154, 103295.
Suzuki, S., Sakaguchi, M., Domen, M., Karato, T., Suzuki, K., 2022. Temperature and ΔK dependence of grain boundary effect on fatigue crack propagation in a two-dimensional polycrystalline Ni-base superalloy. Acta Mater. 240, 118288.
Taylor, D., Knott, J.F., 1981. Fatigue crack propagation behaviour of short cracks; the effect of microstructure. Fatigue Fract. Eng. Mater. Struct. 4, 147–155.
Texier, D., Cormier, J., Villechaise, P., Stinville, J.C., Torbet, C.J., Pierret, S., Pollock, T.M., 2016. Crack initiation sensitivity of wrought direct aged alloy 718 in the very high cycle fatigue regime: the role of non-metallic inclusions. Mater. Sci. Eng. 678, 122–136.
Texier, D., Stinville, J.C., Echlin, M.P., Pierret, S., Villechaise, P., Pollock, T.M., Cormier, J., 2019. Short crack propagation from cracked non-metallic inclusions in a Ni-based polycrystalline superalloy. Acta Mater. 165, 241–258.
Wang, X.S., Fan, J.H., 2006. An evaluation on the growth rate of small fatigue cracks in cast AM50 magnesium alloy at different temperatures in vacuum conditions. Int. J. Fatigue 28, 79–86.
Wang, Z., Guan, K., Gao, M., Li, X., Chen, X., Zeng, X., 2012. The microstructure and mechanical properties of deposited-IN718 by selective laser melting. J. Alloys Compd. 513, 518–523.
Wang, X.Y., Zhao, Y., Wang, L.B., Wei, L.M., He, J.J., Guan, X.F., 2021. In-situ SEM investigation and modeling of small crack growth behavior of additively manufactured titanium alloy. Int. J. Fatigue 149, 106303.
Wang, F.L., Stinville, J.C., Charpagne, M., Echlin, M.P., Agnew, S.R., Pollock, T.M., Graef, M.D., Gianola, D.S., 2023a. Dislocation cells in additively manufactured metallic alloys characterized by electron backscatter diffraction pattern sharpness. Mater. Charact. 197, 112673.
Wang, K., Song, K., Xin, R., Zhao, L., Xu, L., 2023b. Cyclic microstructure analysis, crack propagation and life prediction of Inconel 750H considering the slip fracture energy. Int. J. Plast. 167, 103660.
Wang, S., Ning, Z., Li, P., Li, M., Lin, Q., Wu, H., Chen, G., 2023c. Study on the crack nucleation mechanism of Ti-2Al-2.5Zr alloy in low cycle fatigue: quasi in-situ experiments and crystal plasticity simulation. Int. J. Plast. 165, 103604.
Wen, W., Cai, P., Ngan, A.H.W., Zhai, T., 2016. An experimental methodology to quantify the resistance of grain boundaries to fatigue crack growth in an AA2024 T351 Al-Cu Alloy. Mater. Sci. Eng. 666, 288–296.
Ye, S., Zhang, X.C., Gong, J.G., Tu, S.T., Zhang, C.C., 2017. Multi-scale fatigue crack propagation in 304 stainless steel: experiments and modelling. Fatigue Fract. Eng. Mater. Struct. 40, 1928–1941.
Yu, C.L., Huang, Z.Y., Zhang, Z.A., Shen, J.B., Wang, J., Xu, Z.P., 2021a. Influence of post-processing on very high cycle fatigue resistance of Inconel 718 obtained with laser powder bed fusion. Int. J. Fatigue 153, 106510.
Yu, X.B., Lin, X., Tan, H., Hu, Y.L., Zhang, S.Y., Liu, F.C., Yang, H.O., Huang, W.D., 2021b. Microstructure and fatigue crack growth behavior of Inconel 718 superalloy manufactured by laser directed energy deposition. Int. J. Fatigue 143, 106005.
Zeng, X., Zhang, C., Zhu, W., Zhu, M., Wang, Y., Zhang, X., 2022. Quantitative characterization of short fatigue crack and grain boundary interaction behavior in zirconium. Int. J. Fatigue 161, 106894.
Zhai, T.G., Wilkinson, A.J., Martin, J.W., 2000. A crystallographic mechanism for fatigue crack propagation through grain boundaries. Acta Mater. 48, 4917–4927.
Zhang, X., Dunne, F.P.E., 2023. Short crack propagation near coherent twin boundaries in nickel-based superalloy. Int. J. Fatigue 172, 107586.
Zhang, S.D., Takahashi, Y., 2023. Creep-fatigue life and damage evaluation under various strain waveforms for Ni-based alloy 740H. Int. J. Fatigue 176, 107833.
Zhao, Y., Guo, Q., Ma, Z., Yu, L., 2020. Comparative study on the microstructure evolution of selective laser melted and wrought IN718 superalloy during subsequent heat treatment process and its effect on mechanical properties. Mater. Sci. Eng. 791, 139735.
Zhao, Y., Ma, Z., Yu, L., Dong, J., Liu, Y., 2021. The simultaneous improvements of strength and ductility in additive manufactured Ni-based superalloy via controlling cellular subgrain microstructure. J. Mater. Sci. Technol. 68, 184–190.